A CHANDRA STUDY OF THE MULTICOMPONENT X-RAY EMISSION FROM THE X-SHAPED RADIO GALAXY 3C 403

R. P. KRAFT

Harvard-Smithsonian Center for Astrophysics, 60 Garden Street, MS-67, Cambridge, MA 02138

M. J. HARDCASTLE

School of Physics, Astronomy, and Mathematics, University of Hertfordshire, Hatfield AL10 9AB, UK

D. M. WORRALL

Department of Physics, University of Bristol, Tyndall Avenue, Bristol BS8 ITL, UK

AND

S. S. MURRAY

Harvard-Smithsonian Center for Astrophysics, 60 Garden Street, MS-2, Cambridge, MA 02138

Received 2004 September 28; accepted 2004 December 1

ABSTRACT

We present results from a 49.4 ks *Chandra* ACIS-S observation of the nearby ($z = 0.059$) X-shaped FR type II (FR II) radio galaxy 3C 403. This is the first *Chandra* observation of an X-shaped radio galaxy, and one of the goals of this pioneering study is to determine the relationship between the X-ray–emitting gas and the X-shaped radio morphology. We find that the X-ray isophotes of the hot gas within $\sim 3\rlap{.}''5$ of the central galaxy are highly elliptical (eccentricity ~ 0.57) and coaligned with the elliptical optical isophotes. This supports the hypothesis that X-shaped radio sources are created by propagation of jets through asymmetric density distributions. Within large uncertainties, there is no evidence that the lobes or wings are overpressurized relative to the interstellar medium (ISM), supporting the scenario in which the wings are the result of strong backflows of material from the jet head and subsequent buoyant evolution. We have detected X-ray emission from several of the radio knots to the east of the active nucleus and diffuse emission from the radio lobe to the west. The X-ray emission from the eastern knots cannot be explained by an inverse Compton model unless they are far from equipartition. Using archival *Hubble Space Telescope* (*HST*) data, optical emission is detected from two knots, and the radio/optical/X-ray spectra are well fitted by simple synchrotron models. This is one of the strongest examples to date of X-ray synchrotron emission from multiple knots in the jet of an FR II radio galaxy. X-ray emission is also detected from the radio wings at a flux consistent with inverse Compton scattering of cosmic microwave background (CMB) photons from relativistic electrons if the wings are near equipartition. The nuclear spectrum is well described by a multicomponent model that includes a heavily absorbed power law ($N_H \sim 4 \times 10^{23}$ cm^{-2}) and a bright (EW ~ 244 eV), broadened Fe line. A second, less absorbed, power-law component, likely representing unresolved emission from a parsec-scale jet, is also required.

Subject headings: galaxies: active — galaxies: individual (3C 403) — galaxies: ISM — X-rays: galaxies

1. INTRODUCTION

Approximately 10% of the FR type II (FR II) radio galaxies in the Third Cambridge Revised Catalog of Radio Sources (3CRR) catalog are classified as "X-shaped" or "winged" because of their unusual radio morphologies (Leahy & Williams 1984). These radio galaxies have two pairs of misaligned radio lobes of approximately equal linear extent. They also tend to have low radio luminosities, typically lying near the FR I/FR II division. There are two general hypotheses about the nature and origin of these structures. On the one hand, it has been argued that the X-shaped morphology is essentially a hydrodynamic phenomenon that is the result of supersonic or buoyant flow of radio plasma in an asymmetric gas distribution. Leahy & Williams (1984) and Worrall et al. (1995) argued that the X-shaped radio morphology is a result of strong backflow of material behind the terminal hot spots of radio galaxy jets and subsequent buoyant evolution of the "wings." Capetti et al. (2002) hypothesized that the X-shaped morphology is the direct result of the supersonic expansion/inflation of the lobe into an elliptical atmosphere, and that all radio galaxies in such environments should

exhibit this phenomenon. On the other hand, it has been argued that this structure results from precession or reorientation of the jet axis, possibly as a result of a galaxy interaction and/or merger event of two supermassive black holes (Ekers et al. 1978; Gopal-Krishna et al. 2003; Dennett-Thorpe et al. 2002). In this scenario, the "wings" represent the remnant lobe of an earlier epoch of nuclear activity, and only the primary "jet/lobe" is currently being powered by the nuclear outflow. This latter scenario has generated particular interest recently because it implies that these galaxies may be strong sources of gravitational radiation (Merritt & Ekers 2002).

The sensitivity of *Chandra* and *XMM-Newton* has been a crucial factor in making progress in the study of the gaseous environments of the radio galaxies and better understanding issues related to the dynamics of the radio structures. In addition to emission from the thermal coronae, *Chandra* and *XMM-Newton* observations of radio galaxies have detected dozens of examples of nonthermal X-ray emission from their jets and hot spots. The standard paradigm suggests that the X-ray emission observed from these features has different origins, depending on the power of the radio galaxy. The X-ray emission from the knots of jets of

FR I radio galaxies are generally attributed to synchrotron emission from a population of ultrarelativistic electrons (Worrall et al. 2001). This conclusion is supported by several pieces of evidence, including their broadband spectra. Well-studied examples include Centaurus A (Kraft et al. 2002; Hardcastle et al. 2003), M87 (Marshall et al. 2002), and 3C 66B (Hardcastle et al. 2001). However, inverse Compton (IC) scattering of seed photons by relativistic electrons is generally believed to be responsible for the X-ray emission from jets (Tavecchio et al. 2000; Sambruna et al. 2001) and hot spots (Hardcastle et al. 2004) of the more powerful FR II sources. Well-known hot spot examples include Cygnus A (Carilli et al. 1994) and 3C 295 (Harris et al. 2000). To date, only two examples of X-ray emission from FR II hot spots have been attributed to synchrotron emission, 3C 390.3 (Harris et al. 1998) and Pictor A (Wilson et al. 2001), although Hardcastle et al. (2004) argue that the X-ray emission from a large number of low-power hot spots is at least partly synchrotron in origin.

3C 403 is the nearest X-shaped radio galaxy in the 3CRR catalog (Laing et al. 1983) and is an ideal target to study the X-shaped phenomenon. In this paper, we present results from a *Chandra* observation of this radio galaxy. We use archival VLA and *Hubble Space Telescope* (*HST*) observations to make a multifrequency study of the various components. We have resolved X-ray emission from four distinct components: the bright active nucleus, the hot interstellar medium (ISM), several compact radio components, and diffuse X-ray emission coincident with the radio lobes. This is the first high-resolution X-ray observation of an X-shaped radio galaxy, and the primary goal of this observation was to study the ambient ISM confining the radio-emitting components. In addition, the nonthermal X-ray emission that we detect from several of the compact radio components allows us to draw strong conclusions regarding their emission mechanisms.

This paper is organized as follows. Section 2 contains a brief description of the data, an observation log, and a summary of our analysis. In § 3, we discuss the emission from the hot ISM and nucleus, and we describe how we have separated these components spatially and spectrally. In § 4, we discuss the nonthermal X-ray emission associated with the radio hot spots and lobes. The nature of X-shaped radio galaxies and the implications of our results are discussed in § 5. Section 6 contains a brief summary and conclusion. Throughout this paper, we assume the *Wilkinson Microwave Anisotropy Probe* (*WMAP*) cosmology ($H_0 = 71$, $\Omega_M = 0.27$, and $\Omega_\Lambda = 0.73$), so that the measured redshift of the host galaxy ($z = 0.059$) corresponds to a luminosity distance of 260.6 Mpc and $1'' = 1.127$ kpc.

2. OBSERVATIONS

The radio galaxy 3C 403 was observed for 49,470 s with the *Chandra* ACIS-S instrument (observation ID 2968) in faint mode on 2002 December 12. The nucleus of the galaxy was located at the best focus. The light curve of events in the 5.0–10.0 keV bandpass on the entire S3 chip, excluding the nucleus and any other point sources visible by eye, was created using 259 s bins and examined for periods of flaring background. Intervals in which the rate was more than 3 σ above the mean rate were removed. The mean rate with periods of flaring removed is consistent with the nominal quiescent ACIS-S background listed in the *Chandra* Proposers' Observatory Guide. A total of 4600 s of data were excluded, leaving 44,870 s of good time. Bad pixels, hot columns, and columns along node boundaries were also removed. This galaxy is located at relatively low Galactic latitude ($l = 42°.263$, $b = -12°.314$), so the nominal blank sky background files generated from deep, high Galactic
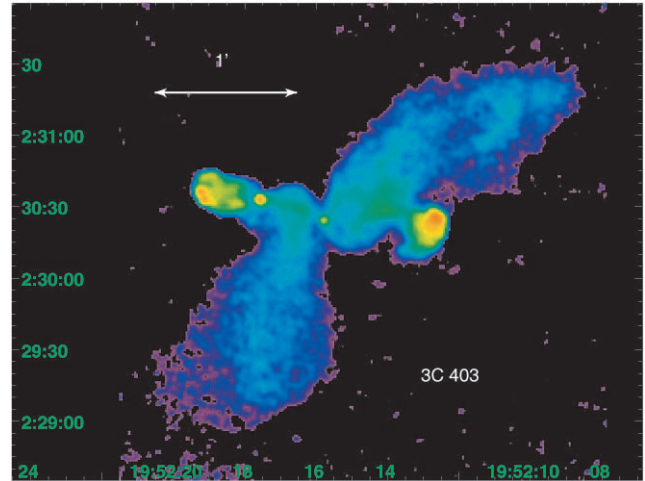

Fig. 1.—8.4 GHz radio map ($0''.75 \times 0''.75$ beam [FWHM]) of 3C 403 (Black et al. 1992). The primary radio lobes and the secondary radio "wings" lie along the east-west and northwest-southeast axes, respectively.

latitude observations are not appropriate. Fortunately, the radio galaxy covers only a small region of the S3 chip, so that local background for spectral analysis was estimated from a large region on the S3 chip north of the source. Absorption by foreground gas in our Galaxy ($N_H = 1.54 \times 10^{21}$ cm^{-2}) was included in all spectral fits.

We have combined data from our *Chandra* ACIS-S observation with archival VLA observations (1.48 and 8.4 GHz) and an *HST* observation to make a multifrequency study of various components. Detailed discussions of the 1.48 and 8.4 GHz VLA data have been presented in Dennett-Thorpe et al. (2002) and Black et al. (1992), respectively. We use the nomenclature of Black et al. (1992) throughout this paper when referring to specific knots or radio features. An 8.4 GHz radio map of this radio galaxy is shown in Figure 1. The primary lobes can be seen to the east and west of the central nucleus. The lower surface brightness "wings" that give this object its X-shaped morphology extend to the north and south. Several hot spots, and perhaps a hint of a jet between the nucleus and knot F6, can be seen in the eastern lobe. The X-ray and radio positions of the active nucleus agree to ~$0''.5$. This radio galaxy was also observed for 280 s with the *HST* WFPC2 instrument in 1995 as part of the *HST* 3CRR snapshot survey using the F702W filter (pivot wavelength of 6919 Å, Martel et al. 1999). We obtained the reprocessed data from the *HST* archive and used the IRAF SYNPHOT package to apply photometric calibrations. The fluxes were reddening-corrected using the dust maps of Schlegel et al. (1998).

An adaptively smoothed, exposure-corrected, background-subtracted X-ray image in the 0.5–2.0 keV bandpass with 8.4 GHz radio contours overlaid is shown in Figure 2. X-ray emission is detected from at least four distinct components: the active nucleus, the hot gas of the host galaxy, several of the radio hot spots, and diffuse emission from the lobes and wings.

3. HOT ISM AND NUCLEUS

A raw X-ray image in the 0.5–2.0 keV bandpass of the central region ($20'' \times 14''$), including the hot ISM and the active nucleus, is shown in Figure 3. The point source at the center is the active galactic nucleus (AGN), and the extensions to the northeast and southwest are the hot ISM. The morphology of the ISM is highly elliptic and coaligned with, but more eccentric
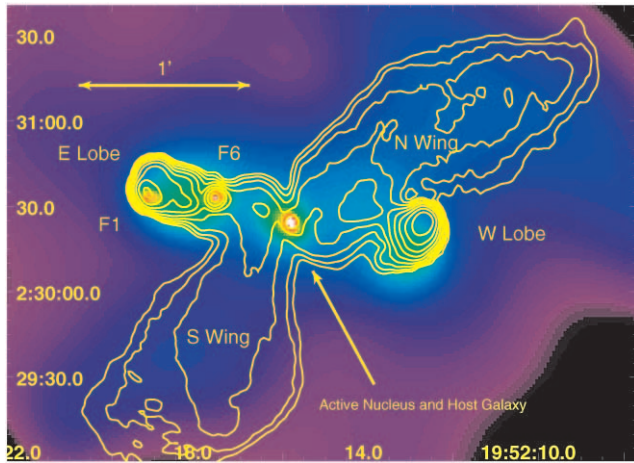
Fig. 2.—Adaptively smoothed, exposure-corrected, background-subtracted *Chandra* ACIS-S image of 3C 403 in the 0.5–2.0 keV band with 8.4 GHz radio contours overlaid. We have detected emission from the active nucleus, the hot ISM, several of the compact radio components, and diffuse emission from the lobes and wings.

Fig. 4.—X-ray spectrum of the central $7\farcs5$ radius region with best-fit model overlaid. The residuals are plotted in the bottom panel. The best-fit parameters and uncertainties are summarized in Table 1. This spectrum includes emission from the unresolved core and the hot ISM.

than, the optical isophotes of the stellar light distribution (Capetti et al. 2002). We wish to separate the emission of the hot ISM from that of the active nucleus in order to study each component separately. Unfortunately, these components are not well separated spatially. The major and minor axes of the ISM shown in Figure 3 are approximately $7\farcs5$ and $3\farcs0$ in length, respectively. The 90% encircled energy radius for a point source on-axis at 1.49 keV is $\sim 0\farcs9$. We have used images in four X-ray bands to guide our spectral analysis in order to separate the emission from the two components. An examination of images in the 0.5–0.7, 0.7–1.0, 1.0–1.5, and 1.5–2.0 keV bands showed that above 1 keV, most of the emission is unresolved and is probably due to the active nucleus. Below 0.7 keV, the contribution from the central point source is small, and most or all of the emission is from the ISM.

We extracted the spectrum, shown in Figure 4, from a $7\farcs5$ radius circular region centered on the nucleus. The data have been binned to a minimum of 10 counts per bin, and the background was determined from a large region on the S3 chip approximately $4'$
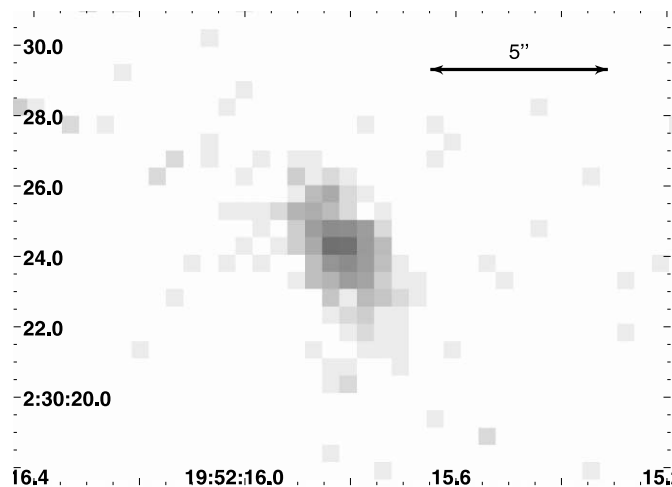

Fig. 3.—Raw *Chandra* ACIS-S image of the central $20'' \times 15''$ region of 3C 403. The unresolved point source is at the center, and the emission of the hot ISM extends to the northeast and southwest of the nucleus. The brightest pixel contains 63 events, and there are 515 total in the image.
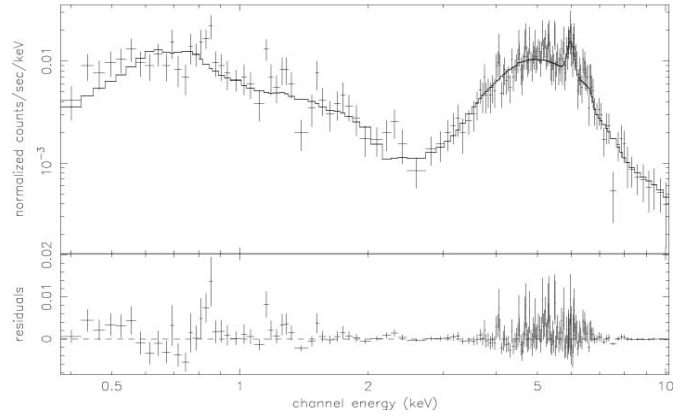
to the north of the nucleus, well removed from any detectable emission from the galaxy. The spectrum consists of two peaks: one centered at ~ 0.7 keV with a high-energy tail, and a second that peaks at ~ 5 keV. The count rate in the 0.25–10.0 keV band was 4.7×10^{-2} counts s^{-1}. The majority of the counts in this spectrum are from the unresolved active nucleus. This suggests that this spectrum moderately suffers from the effects of pileup. Based on Figure 6.19 of the *Chandra* Proposers' Observatory Guide, we estimate a pileup fraction of $\sim 5\%$. We note that we fitted the data using coarser binning (25 and 50 counts per bin) to ensure the applicability of Gaussian statistics and find statistically identical parameter values and uncertainties.

We initially modeled the spectrum with a three-component model including a heavily absorbed ($N_H > 10^{23}$ cm^{-2}) power law, an Fe line with variable centroid and width, and an APEC model. The effect of the pileup was modeled using the XSPEC function *pileup* (Davis 2001), and Galactic absorption ($N_H = 1.54 \times 10^{21}$ cm^{-2}) was included in all fits. For simplicity, the elemental abundance of the APEC model was fixed at 1.0 times solar, typical of the central regions of early-type galaxies. If allowed to vary freely, the elemental abundance was poorly constrained. At the relatively low best-fit temperature (~ 0.3 keV), the emission is line-dominated, and the elemental abundance can be traded against the normalization. The radiative cooling function, $\Lambda(T, Z)$, scales nearly linearly with abundance at these temperatures and abundances. None of our conclusions are sensitive to this choice, although a larger elemental abundance would reduce our estimates of the gas density ($n_H \sim Z^{-1/2}$).

In this scenario, the power law represents emission from the AGN, and the APEC model represents the emission from the hot ISM. We could not obtain an acceptable fit with this three-component model, as there were large residuals between 1 and 2 keV. Inspection of images in the 1–2 keV band suggests that most of the emission in this band is due to the unresolved AGN. We therefore added a second, less absorbed power law to the model and were able to obtain an acceptable fit. An examination of the images in several bands (described above) suggests that this second power law is heavily absorbed. We fixed the absorption and spectral index of this second power law to 4×10^{21} cm^{-2} and 2.0, respectively, to minimize the number of free parameters; only the normalization of this component was allowed to vary freely. The choice of a spectral index that is steeper than that of the primary absorbed power law and the choice of the value of N_H constrain this component to contribute little above and below
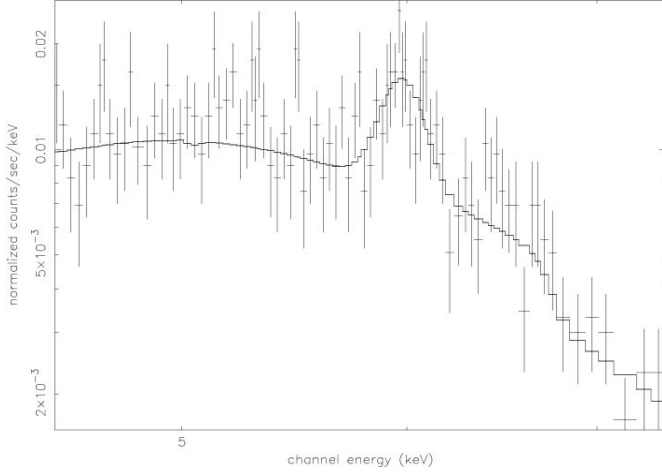
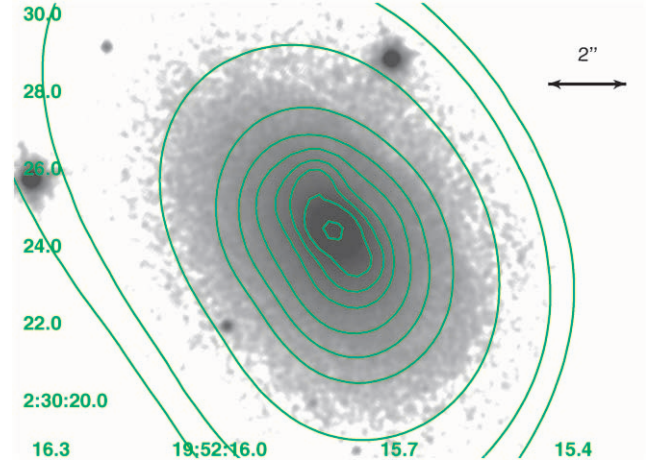Fig. 5.—Data and best-fit model X-ray spectrum of the central 7″.5 radius region around the Fe K line.

Fig. 6.—Contours from an adaptively smoothed X-ray image in the 0.3–1.0 keV bandpass overlaid onto an *HST* WFPC2 image of the host galaxy of 3C 403. The ellipticity and angle of rotation of the optical and X-ray isophotes are consistent.

the 1–2 keV band. The best-fit model has been overlaid onto Figure 4. The data and model around the Fe K line are more clearly shown in Figure 5. The best-fit values of the parameters and 90% confidence intervals are summarized in Table 1.

3.1. *ISM*

The morphology of the X-ray emission of the central region of the hot ISM is highly elliptical and coaligned with the optical isophotes of the host galaxy. We have overplotted the contours from an adaptively smoothed X-ray image in the 0.5–2.0 keV band onto an *HST* WFPC2 image of the host galaxy, as shown in Figure 6. The position angle of the diffuse emission is not aligned with the primary east-west radio components and is almost perpendicular to the northern and southern radio wings. The spatial relationship between the lobes, the wings, and the

TABLE 1
SUMMARY OF SPECTRAL PARAMETERS FOR NUCLEUS AND HOT ISM

Parameter	Value
Count rate...	4.71×10^{-2} counts s^{-1}
APEC:	
$k_B T$...	0.3 ± 0.04 keV
Z..	$1.0 \times$ solar (fixed)
N_H...	1.54×10^{21} cm^{-2} (fixed, Galactic)
Flux	3.6×10^{-14} ergs cm^{-2} s^{-1}
Luminosity (L_X)............................	2.9×10^{41} ergs s^{-1}
First power law:	
Index	1.70 ± 0.15
N_H...	$(4.0 \pm 0.2) \times 10^{23}$ cm^{-2}
Flux	1.31×10^{-11} ergs cm^{-2} s^{-1}
Luminosity (L_X)............................	1.07×10^{44} ergs s^{-1}
Second power law:	
Index	2.0 (fixed)
N_H...	4.0×10^{21} cm^{-2} (fixed)
Flux	8.75×10^{-14} ergs cm^{-2} s^{-1}
Luminosity (L_X)............................	7.11×10^{41} ergs s^{-1}
Fe line:	
Centroid...	6.31 ± 0.04 keV
Width (rms)....................................	80 ± 50 eV
EW	244 ± 20 eV

NOTE.—All uncertainties are at 90% confidence. The count rate is in the 0.25–10.0 keV band. The fluxes and luminosities listed for each component are unabsorbed in the 0.25–10.0 keV band. The equivalent width of the Fe line is relative to the first power-law component.

ISM, at least near the nucleus, is qualitatively what we would expect in the buoyancy/backflow model. Based on the spectral analysis above, the unabsorbed X-ray luminosity of the ISM within 8.5 kpc of the nucleus is 2.9×10^{41} ergs s^{-1} in the 0.25–10.0 keV bandpass. This X-ray luminosity is at the high end of the L_X versus L_B relationship derived from observations of large samples of elliptical galaxies in Canizares et al. (1987) and O'Sullivan et al. (2001). The temperature of the gas in this central region is ~0.3 keV, which is rather low for a massive elliptical galaxy, perhaps indicative of a cooling flow.

We fitted an elliptical β-model plus constant background to an X-ray image of the central 5″ of the galaxy in the 0.3–1.0 keV bandpass using the Sherpa software package in order to quantitatively characterize the morphology of this emission. As demonstrated above, the contribution from the nucleus in this band is small. The free parameters of this model were β, the scale parameter r_0, the normalization, the ellipticity ϵ, the position angle of the major axis of the ellipse θ, and the background B. The telescope point-spread function (PSF) was computed using the CIAO program *mkpsf* to remove the instrumental response. Both ϵ and θ were well constrained, with $\epsilon = 0.57 \pm 0.04$ and $\theta = 44° \pm 2°$ (measured east of north). The uncertainties are at 90% confidence. Based on the spectral analysis described above, the 0.3–1.0 keV band contains little emission from the active nucleus. The parameters β and r_0 were poorly constrained, but $\beta > 0.5$ and $r_0 < 3″$ (<3.5 kpc). Using nominal values of $\beta = 0.55$ and $r_0 = 0″.6$, the central proton density, n_0, is ~1.14 cm^{-3} for the best-fit spectrum described above. The values of r_0 and n_0 are somewhat smaller and larger, respectively, than those typically observed in elliptical galaxies, although it is not uncommon to find small-scale, dense cores in the ISM at the centers of radio galaxies (Hardcastle et al. 2002). The cooling time of this material is very short, ~10^7 yr, because of the high density and relatively low temperature. A metal abundance higher than what we have assumed (1.0 times the solar value) would decrease the central density but shorten the cooling time (the cooling time scales roughly as $Z^{-1/2}$).

On the kiloparsec scale, the X-ray morphology, and presumably the density and pressure profiles, are highly elliptical ($\epsilon = 0.57$). In contrast, the ellipticity of the stellar light profile is only 0.25 at 6″.9 (the effective radius of the de Vaucouleurs profile for the host of 3C 403) from the nucleus (Govoni et al.

2000). We have detected X-ray emission to only half this distance along the semimajor axis, but an examination of the central 3″ of the *HST* images clearly shows that the stellar distribution has a roughly constant ellipticity (~0.25) down to about 1″, where the distribution becomes circular. The distribution of the gas is therefore more elliptical than that of stars. In the central 10–15 kpc of elliptical galaxies, the stellar mass typically dominates the dark matter, so the gravitational potential should be determined by the distribution of the former. If the gas is in hydrostatic equilibrium with the gravitating matter, we expect that the ellipticity of the gas and that of the gravitating matter should be similar, but in fact this is not the case in 3C 403.

We suggest two possible explanations for this. The first, and most likely in our view, is that the gas is not in hydrostatic equilibrium. The cooling time of this gas is less than 10^7 yr, roughly the same age as the radio lobes. It is plausible that the gas is cooling and falling in toward the center. The inflation of the radio lobe may have disrupted the central region as well. If the gas is moving, it may well have a different morphology than the gravitating matter. As an alternative, it is possible that the emission that we have been attributing to the ISM is, in fact, due to a partially resolved kiloparsec-scale jet. We consider this unlikely for two reasons. First, there is no evidence for any radio counterpart to this emission. The X-ray–to–radio spectrum would have to be unusually flat. Second, the axis of this hypothetical kiloparsec-scale jet is not aligned with the larger scale (tens of kiloparsecs) radio features, which implies that the jet has been sharply bent.

On larger (tens of kpc) scales, the data are not of sufficient quality for us to determine whether the gas distribution remains elliptical at or beyond the boundaries of the wings and lobes. We can, however, address the simpler question of whether the radio wings are greatly overpressurized relative to the ambient medium. There is statistically significant emission above background out to about 50″ from the nucleus, although the profile of the emission is poorly constrained. This could represent emission associated with a group of galaxies for which the optical host of 3C 403 is the dominant member. However, the surface brightness profile of the gas from the core to ~50″ cannot be described by a single β-profile. Given the small core radius and high density of the emission in the central region, it is not reasonable simply to extrapolate this to larger radii to estimate the gas pressure for a comparison with the pressure of the lobes and wings. For simplicity, and because it would be difficult to maintain a gas distribution to large radii that is more elliptical than the stellar mass distribution, we assume that the profile is spherically symmetric and parameterize the data with a circular β-profile. We note that using an elliptical profile (e.g., with the same ellipticity that we found for the smaller scale emission) would not significantly change our conclusions. A plot of the surface brightness in circular annuli versus distance from the nucleus is shown in Figure 7. X-ray knots, hot spots, and background point sources have been excluded.

We measure a flux of 1.32×10^{-14} ergs cm^{-2} s^{-1} (unabsorbed) in the 0.1–10.0 keV band in an annular region 50″ in radius from the nucleus, excluding the central 10″. The X-ray luminosity of this emission is $\sim 1.1 \times 10^{41}$ ergs s^{-1} in the same band. We have assumed a gas temperature of 0.7 keV, typical for groups, and an elemental abundance of 0.4 times solar. For an assumed spherical β-model profile with $\beta = 0.5$ and $r_0 = 30''$, the central proton density is $\sim 3.3 \times 10^{-3}$ cm^{-3}. The gas pressure at the distance of the center of the wings is $\sim 2 \times 10^{-12}$ dyn cm^{-2}. The equipartition pressure of the wings is
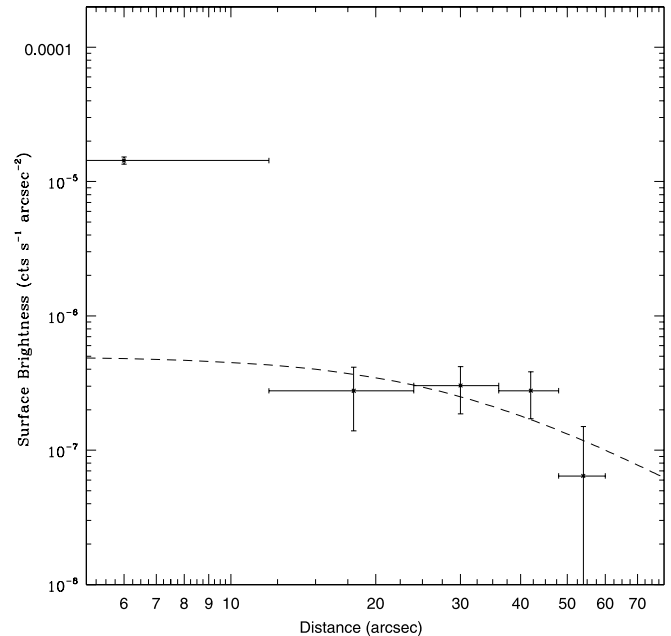

Fig. 7.—Radial surface brightness profile (background-subtracted) in circular annuli of the larger scale (tens of kpc) diffuse emission of 3C 403 in the 0.3–1.0 keV band. All the point sources, knots, and diffuse emission from the western radio lobe have been removed. The surface brightness of the background is 6×10^{-7} counts s^{-1} arcsec^{-2} and was estimated from a 1′.5 radius circular region ~4′ to the north of the nucleus. The dashed curve represents the best-fit β-profile, excluding the first data point.

$\sim 5 \times 10^{-13}$ dyn cm^{-2} (see § 4.2). If all of the X-ray emission from the wings is due to IC scattering of cosmic microwave background (CMB) photons, the pressure is $\sim 1 \times 10^{-12}$ dyn cm^{-2} (see below). Thus, the internal minimum pressure of the radio wings is the same order of magnitude as the pressure of the ambient medium. Our estimate of the gas pressure has large uncertainties, and we have ignored the effects of projection, which would place the lobes further out into the halo and into lower density gas. Given the uncertainties, it is reasonable to conclude that the lobes are in approximate pressure equilibrium with the ISM. There is no evidence to suggest that the wings are greatly overpressurized relative to the ambient medium.

3.2. *Active Nucleus*

The spectrum of the nucleus is well described by a two–power-law model plus an Fe line. The primary power law is heavily absorbed ($N_{\rm H} \sim 4 \times 10^{23}$ cm^{-2}). We attribute the primary power-law component to emission from material near the inner part of the accretion, close to the central supermassive black hole. There is no evidence for a significant amount of dust in *HST* observations of the host galaxy (Martel et al. 1999), so it is likely that this large absorption column is due to cool material in close proximity to the central black hole, perhaps a molecular torus. This is consistent with previous optical emission line studies that have shown that 3C 403 is a narrow emission-line galaxy (NELG, Tadhunter et al. 1993, 1998). This suggests that we are observing the disk/torus nearly edge-on, and that the jets are advancing at an angle close to the plane of the sky. The broad-line region, if it exists, must be buried behind the torus and unobservable. Neither the photon index (1.7 ± 0.15) nor the unabsorbed X-ray luminosity (1.07×10^{44} ergs s^{-1} in the 0.25–10 keV bandpass) are unusual for the nuclei of radio galaxies.

The parameters of the second power-law component are poorly constrained, and as described above, we have fixed the power-law index ($\alpha = 2$) and absorption ($N_{\rm H} = 4 \times 10^{21}$ cm^{-2}) of this component for consistency with the imaging data. We suggest that this second power-law component is X-ray emission from an unresolved jet that is partially obscured, as observed with greater sensitivity in Centaurus A (Evans et al. 2004). The radio luminosity of the core is 6.5×10^{21} W Hz^{-1} sr^{-1} at 5 GHz. The X-ray luminosity of the second power-law component is 7.1×10^{15} W Hz^{-1} sr^{-1} at 1 keV. The X-ray–to–radio flux ratio is consistent with that found in a sample of low-power radio galaxies (Canosa et al. 1999) and supports the hypothesis that this second power-law component is related to spatially unresolved emission from a jet. It is likely that the excess column density is due to absorption within a few parsecs of the nucleus. We speculate that this unresolved jet lies above the accretion disk, and our line of sight to the jet passes through a region of lower column density higher up in the torus. There is no evidence of gas or dust on kiloparsec scales, perhaps from a recent merger, that could be responsible for this large column. It is also possible that the hot ISM is responsible for this large column. The column density of the hot gas within a distance r_0 (the central core radius) is $N_{\rm H}^{\rm ISM} = r_0(1 - \epsilon)n_0 \sim 1.0 \times 10^{21}$ cm^{-2}, remarkably close to the 4×10^{21} cm^{-2} value chosen based on the multiband images. A careful calculation would require detailed knowledge of the ionization state of the gas, the distribution of gas along the line of sight, and the elemental abundance, all of which are poorly constrained. Alternatively, it is possible that this second power-law component is due to either electron scattering from an ionized corona or a partial covering fraction absorber, both of which are often invoked to explain the X-ray spectrum of Seyfert galaxies (Turner et al. 1997). The observed flux ratio of the first and second power-law components is consistent with that observed in Seyfert galaxies. The jet hypothesis is, however, more natural in our view, as 3C 403 is an FR II radio galaxy. This hypothesis could be evaluated by a VLBI observation to search for a parsec-scale jet near the core.

A strong Fe line with EW $= 244 \pm 20$ eV (90% confidence) has also been detected. The centroid of the line is 6.31 ± 0.04 keV, and the width (rms) of the line is 80 ± 50 eV. The centroid of this line is consistent with fluorescent emission from cold material. The large EW of this line is consistent with a model in which the line emission originates from an absorbing region that surrounds the central supermassive black hole (Leahy & Creighton 1993; Miyazaki et al. 1996). The measured width of the Fe line corresponds to a velocity (FWHM) of 900 km s^{-1}. If the line broadening is the result of fluorescence from cold gas in Keplerian motion around a $10^9 \, M_\odot$ black hole, it must lie $\sim$5 pc from the black hole. It is reasonable to attribute the large column and fluorescent Fe line to a molecular torus that surrounds the central supermassive black hole.

4. EXTENDED RADIO-RELATED X-RAY EMISSION

As shown in Figure 8, small-scale X-ray emission is associated with multiple radio components in the eastern lobe: these include the radio components F7/F8, F6, F5, F1, and a distinct radio component upstream of F1, which we denote F1b. There is no detected X-ray emission associated with the hot spot components F2 or F3 in the eastern lobe or with the larger hot spots P1 and P2 in the western lobe. Figure 9 shows that there is also large-scale diffuse emission associated with the western lobe and with both the extended wings. The position of the active nucleus in the X-ray data using the nominal aspect solution
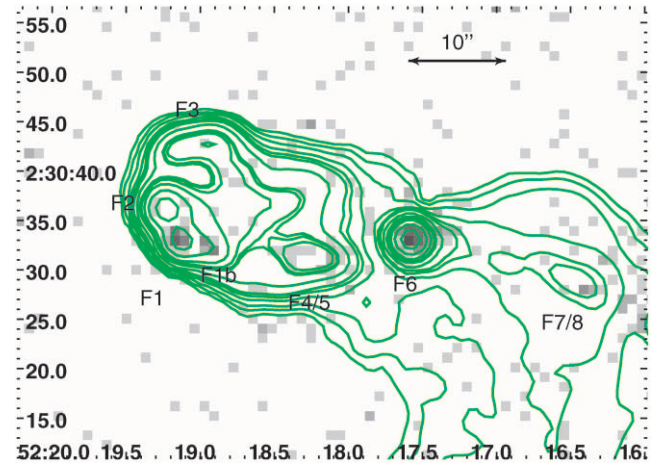

FIG. 8.—Raw X-ray image (1 pixel $= 0\farcs984$) in the 0.5–2.0 keV bandpass with 8.4 GHz radio contours overlaid. We clearly detect X-ray emission from radio knots F1, F4/5, and F6 and the jetlike feature F7/8. The X-ray emission from knot F6 is clearly extended, but the radio emission is pointlike. We also detect a pointlike source of X-rays $\sim$4$''$ from radio knots F1 but closer to the nucleus. There is no clear radio knot corresponding to this X-ray knot. We have labeled this feature F1b. The radio contours correspond to flux densities of 0.18, 0.35, 0.6, 0.9, 1.4, 2.0, 3.3, 4.4, 11.5, 22.0, and 35.0 mJy beam^{-1}. The resolution of the radio data is $0\farcs75 \times 0\farcs75$.

agrees with the radio position to better than $0\farcs5$. We have not attempted to improve the aspect solution beyond this.

4.1. Compact Components

We begin by considering the compact components in the eastern lobe, shown in Figure 8. For the X-ray emission associated with the radio hot spots F1 and F6, there are enough counts to fit a power-law spectrum. We find best-fitting photon indices of $1.75^{+0.4}_{-0.3}$ and $1.7^{+0.3}_{-0.2}$ for F1 and F6, respectively, and normalizations corresponding to flux densities at 1 keV of 0.9 ± 0.2 and 2.3 ± 0.2 nJy, respectively. For the other three compact components, there are not enough counts to extract a spectrum, so we estimated the flux densities based on the count rates, assuming a photon index of 2. (The flux density is insensitive to our assumed photon index: for a photon index of 1.5, the flux densities would decrease by $\sim$10%.) Flux densities for all the eastern lobe components are tabulated in Table 2.

We use the 8.4 GHz maps (Black et al. 1992) to measure radio flux densities corresponding to the X-ray detections. For compact radio components, it is possible to extract radio flux densities either by integrating over the whole X-ray extraction region (with local background subtraction) or by fitting a model, such as a homogeneous sphere (as was done by Hardcastle et al. 2004) or a Gaussian. In Table 2 we tabulate radio flux densities extracted using both methods when they were both possible, which is true of the compact components F1 and F6; this illustrates the range of possible radio flux densities that can be said to correspond to the X-ray emission. We also tabulate the ratio of X-ray–to–radio flux.

The compact components F1 and F6 are detected with *HST*; the *HST* image with X-ray contours overlaid is shown in Figure 10. The radio through X-ray spectra of these two knots are shown in Figure 11. We have fit synchrotron models to these data, and both of these components are well fitted by a single standard continuous injection model (Heavens & Meisenheimer 1987). As pointed out by Hardcastle et al. (2004), inverse Compton models require extreme conditions to reproduce the observed X-ray flux densities. The knots must either be far from equipartition, or
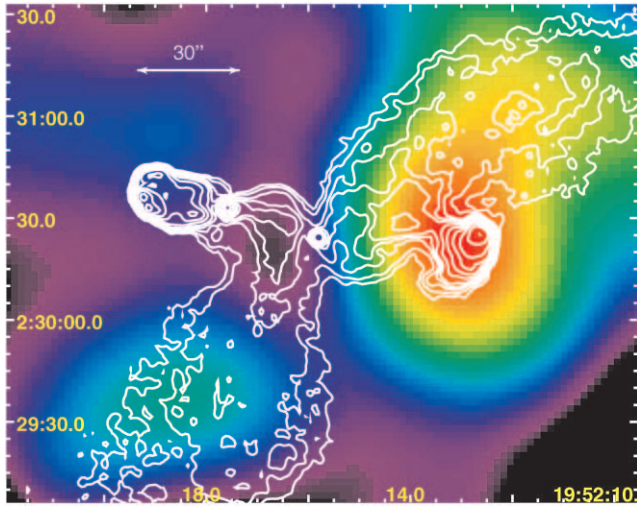
Fig. 9.—Gaussian-smoothed ($\sigma = 20''$), exposure-corrected, background-subtracted X-ray image in the 0.5–2.0 keV bandpass with all small-scale features, including the nucleus, knots, and central ISM, removed. Radio contours (8.4 GHz) are overlaid. The low surface brightness diffuse X-ray components associated with the wings and the western radio lobe are visible. The orange, green, and blue regions correspond to surface brightnesses of 3.2×10^{-3}, 1.9×10^{-3}, and 1.0×10^{-3} counts s^{-1} arcmin^{-2}, respectively. The radio contours correspond to flux densities of 0.2, 0.4, 0.6, 1.1, 1.5, 2.5, 4.5, 12.0, 20.0, and 30.0 mJy beam^{-1}. The resolution of the radio data is $2''.5 \times 2''.5$.

they must be moving relativistically at an angle close to the line of sight. A synchrotron model seems to be the only plausible explanation for the X-ray emission from F1 and F6. For the other components, the existing short *HST* observation does not give us useful constraints (these features are resolved at 8.4 GHz with a $0''.25$ beam and therefore spread over many *HST* WFC pixels), and we do not have X-ray spectral measurements. However, the radio–to–X-ray ratios for the other detected components (Table 2) are very similar to those measured for F1 and F6, so it would seem plausible that they have the same emission mechanism.

An interesting feature of this interpretation is that some of the X-ray–detected components of 3C 403 are morphologically part of the jet rather than being hot spots: this is true of F1b, F5/4, and (the clearest case) F7/8, and it is also debatable whether F6 should be considered a jet knot rather than a primary hot spot. X-ray emission from hot spots is, of course, seen in many other sources and has been attributed to synchrotron emission in some cases (e.g., 3C 390.3, Harris et al. 1998), although 3C 403 is one of the clearest cases of synchrotron rather than inverse Compton emission (Hardcastle et al. 2004). However, 3C 403 is one of the best examples of synchrotron X-ray emission from the jet
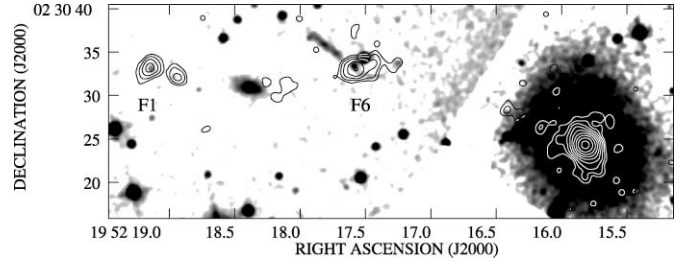

Fig. 10.—Mosaic *HST* image of knots F1 and F6 with X-ray (0.5–5.0 keV band) contours overlaid. The host galaxy is seen to the west. The X-ray data have been smoothed with a $0''.5$ (FWHM) Gaussian.

of a powerful *narrow-line* radio galaxy. In unified models of FR II radio galaxies, the jets of narrow-line radio galaxies are at large angles to the line of sight (Barthel 1989); this is true even for lower luminosity objects, whose unification partners must be broad-line radio galaxies rather than quasars (Hardcastle et al. 1998a, 1999). In both cases, the numbers of the different classes of objects observed require that the narrow-line objects be at angles greater than $45°$ to the line of sight. Such large angles effectively rule out the possibility of applying the popular beamed inverse Compton model (Tavecchio et al. 2000) to the jet in 3C 403. We have calculated the expected flux density in this model for the jet component F7/8 for a range of angles and bulk Lorentz factors and find that the observed flux density can only be reproduced with large bulk Lorentz factors ($\Gamma > 7$) and small angles to the line of sight ($\theta < 8°$). While the large bulk Lorentz factors cannot be ruled out, such small angles to the line of sight are inconsistent with everything that is known about 3C 403. A synchrotron model appears to be the only viable one here. It is unclear what fraction of FR II jets are dominated in the X-ray band by synchrotron emission, but they may be common. The inverse Compton process may dominate only in those sources whose jets are highly beamed.

Finally, we wish to draw attention to two other interesting features of the compact X-ray emission. The first is the non-detection of the hot spot component F2. The upper limit on the X-ray emission from this hot spot is an order of magnitude below the level at which it would have been detected if its radio–to–X-ray ratio had been the same as the detected components'. In a synchrotron interpretation, this requires a difference in the particle acceleration properties of F1 and F2. It is possible that F2 is a relic hot spot that is now detached from the jet flow and that has no ongoing particle acceleration. The second interesting feature is the clear extension of the brightest X-ray feature, F6, back toward the nucleus. Figure 12 contains

TABLE 2
X-Ray and Radio Flux Densities for Compact Components in the Eastern Lobe

| Name | 0.5–5.0 keV Counts | X-Ray Flux Density at 1 keV (nJy) | Photon Index | Radio Flux at 8.4 GHz | | X-Ray/Radio Ratio (10^6) |
				Model (mJy)	Integrated (mJy)	
F1	34 ± 6	0.9 ± 0.2	$1.75^{+0.4}_{-0.3}$	16	25	0.06–0.04
F1b	15 ± 4	0.5 ± 0.1	2	...	7.7	0.06
F2	<4	<0.13	2	...	27	<0.004
F5/4	14 ± 4	0.5 ± 0.1	2	...	10.8	0.05
F6	83 ± 9	2.3 ± 0.2	$1.7^{+0.3}_{-0.2}$	27	41	0.09–0.06
F7/8	9 ± 3	0.3 ± 0.1	2	...	2.6	0.12

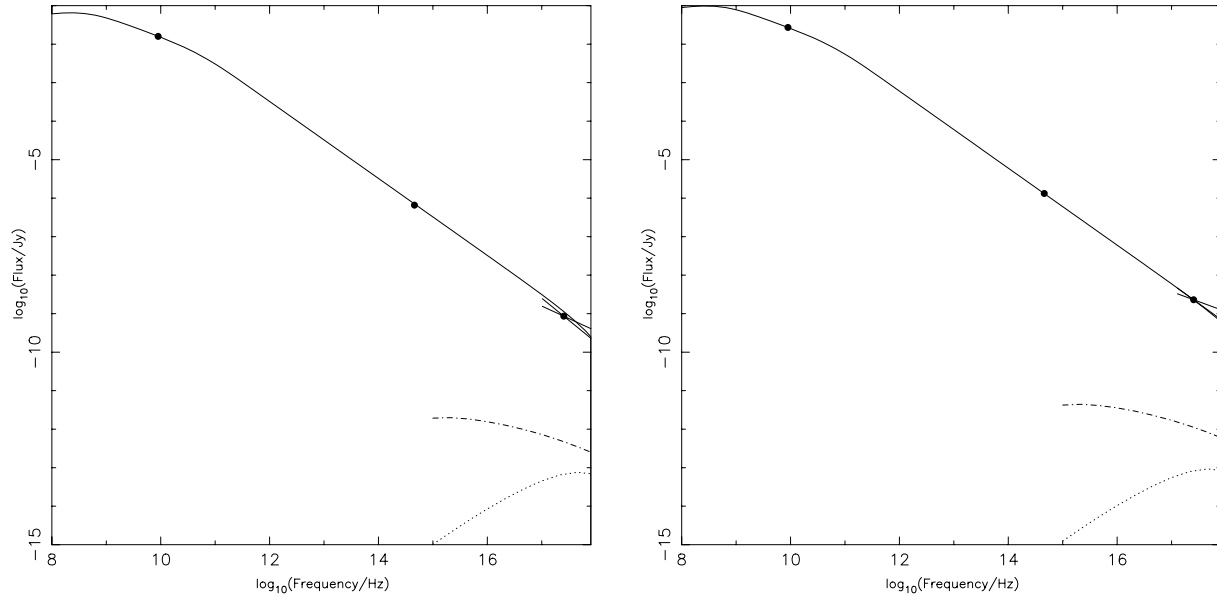Note.—The radio–to–X-ray photon index was assumed to be 2 unless otherwise stated.

Fig. 11.—Radio through X-ray spectrum of knots F1 (*left*) and F6 (*right*), both fitted with a standard continuous injection electron spectrum (Heavens & Meisenheimer 1987) with an electron energy break at an electron Lorentz factor $\gamma = 14,000$ and a minimum energy corresponding to $\gamma = 1000$ and assuming an equipartition magnetic field strength. The dot-dashed and dotted lines show the contributions expected from synchrotron self-Compton emission and inverse Compton scattering of the CMB, respectively.

an X-ray image of the knot F6 in the 0.5–2.0 keV band, with 8.4 GHz radio contours overlaid. The peaks of the radio and X-ray emission are well aligned, and both knots are clearly extended. The X-ray extension is to the west of the main peak, and the radio extension is to the southwest. There is no clear radio counterpart to the X-ray extension, and if the extension is considered to be radio related, it has an X-ray–to–radio flux density ratio more than a factor 10 above most of the other features in the jets (based on an upper limit to the possible associated radio emission). This sort of X-ray–to–radio ratio is not impossible for a synchrotron feature—knots in the Centaurus A jet show similar properties—but its location just upstream of a bright hot spot or jet knot is certainly intriguing and reminiscent of the "offsets" seen in the jets of FR I radio galaxies (Kraft et al. 2002; Hardcastle et al. 2003).
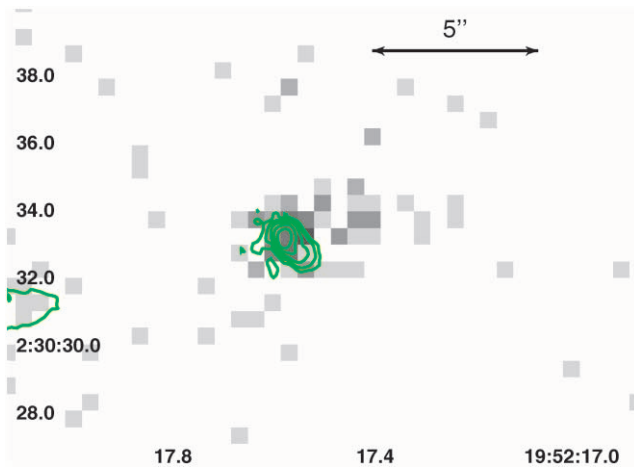

Fig. 12.—Raw X-ray image (1 pixel = 0″.492) of knot F6 in the 0.5–2.0 keV bandpass with 8.4 GHz radio contours overlaid. Note the X-ray extension to the west of the main peak and the radio extension to the southwest. The radio contours correspond to flux densities of 0.04, 0.2, 0.6, 2.0, and 4.0 mJy beam^{-1}. The resolution of the radio data is 0″.25 × 0″.25.

4.2. Extended Components

Extended X-ray emission from the lobes of FR II radio sources is normally attributed to inverse Compton emission (e.g., Hardcastle et al. 2002; Brunetti et al. 2002; Isobe et al. 2002; Comastri et al. 2003; Belsole et al. 2004; Croston et al. 2004). Typically, the X-ray flux densities measured from the lobes are close to, or slightly above, the value expected for inverse Compton scattering of the microwave background radiation by lobes with magnetic field strengths close to the equipartition value. The detected extended emission from the western lobe and wings of 3C 403 is too faint and diffuse for us to fit a spectrum, so that we cannot test the inverse Compton model's prediction of a flat (photon index of 1.5) X-ray spectrum. However, we can estimate the 1 keV flux densities of the various components from the observed count rate. Here we assume a photon index of 1.5 in converting between counts and flux density. The results are tabulated in Table 3. The X-ray counts are background subtracted, and the uncertainties are statistical (Poisson).

We measured corresponding radio fluxes from 1.4 and 8.4 GHz radio maps (the low-resolution map of Black et al. [1992] and a map made from the 1.4 GHz B configuration data of Dennett-Thorpe et al. [2002]). These are also tabulated in Table 3. Modeling the lobes and hot spots as being in the plane of the sky, we then calculated the expected inverse Compton flux density at equipartition. To do this, we assumed no relativistic protons, a low-energy electron energy cutoff corresponding to $\gamma = 10$, and a low-energy electron energy index of 2 (corresponding to $\alpha = 0.5$). A high-energy break and cutoff were included to fit to the steep spectral index between 1.4 and 8.4 GHz, and the radio spectra were normalized to the appropriate fraction of the 178 MHz flux density of 28.3 Jy (see Leahy et al. 1997); this is justified given the very uniform spectral index found by Dennett-Thorpe et al. (2002). The inverse Compton calculation was then carried out using the code of Hardcastle et al. (1998b). We have assumed cylindrical geometry for the wings and spherical geometry for the western lobe. The results are tabulated in Table 3.

TABLE 3
Flux Densities and Predictions for the Extended Components of 3C 403

| Name | 0.5–5.0 keV Counts | Flux | | | Geometry[a] | Predicted IC at 1 keV | Ratio Observed/Predicted |
		1 keV (nJy)	1.4 GHz (Jy)	8.4 GHz (Jy)		(nJy)	
N wing	63 ± 29	1.6	0.78	0.27	cylinder, $90'' \times 24''$	0.35	4.6
S wing	53 ± 28	1.4	0.71	0.24	cylinder, $90'' \times 25''$	0.34	4.0
W lobe	55 ± 14	1.4	1.88	0.50	sphere, $7\rlap{.}''5$	0.1	14

[a] The cylinder and sphere dimensions are length × radius and radius, respectively.

The ratios of observed to predicted X-ray flux are around 4 for the two wings, which is not particularly unusual for radio galaxies (Croston et al. 2004) and suggests field strengths within a factor of ~ 2 of the equipartition value in the wings. The discrepancy with the equipartition prediction would be further reduced if there were any projection of the wings. If we assume no projection and take the X-ray flux density as giving a magnetic field strength measurement, then the electron energy density dominates over the magnetic field energy density in these lobes by around a factor of 20, and the nonthermal pressure in the wings is about 10^{-12} dyn cm^{-2} (with large uncertainties because of the large formal error on the count measurement). The western lobe, on the other hand, has a ratio of observed to predicted flux that is much larger than is typical, and the distribution of X-ray counts in this region is also not what would be expected from a simple inverse Compton model, in which it should more or less match the low-frequency radio emission (Fig. 11). The X-ray emission is not peaked at the radio peak in the northern end of the lobe; rather, the X-ray emission uniformly fills the lobe. Therefore, this emission cannot be explained by inverse Compton scattering of CMB photons by the electrons responsible for the radio emission. Because of the differences in radio and X-ray morphology, this emission is unlikely to be a shock-heated shell of gas surrounding the lobe that would be created if the lobe were expanding into the ISM supersonically (Heinz et al. 1998; Kraft et al. 2003). It is possible that the X-ray emission from the western lobe is due to inverse Compton scattering of beamed IR/optical photons from the active nucleus by a lower energy, unobservable population of relativistic electrons. Such a model has been used to explain diffuse X-ray emission from the western lobe of the quasar 3C 207 (Brunetti et al. 1997, 2002).

5. DISCUSSION—THE NATURE OF X-SHAPED RADIO GALAXIES

As summarized in the introduction, there are two general scenarios commonly invoked to explain the X-shaped morphology of radio galaxies such as 3C 403. One line of argument suggests that the X-shaped morphology is a hydrodynamic phenomenon, and the other is that X-shaped radio galaxies are formed as the result of a sudden change in the jet axis of AGNs, perhaps as the result of a galaxy merger and/or the merger of two supermassive black holes. Within the hydrodynamic scenario, there are two general models in the literature: the X-shaped structure is the result of strong (perhaps highly supersonic) backflow and subsequent buoyant evolution (Leahy & Williams 1984; Worrall et al. 1995), or both the lobes and wings are highly supersonic (relative to the ambient ISM/ICM), and the observed structures are the natural result of overpressurized expansion/inflation of the lobes into an asymmetric medium (Capetti et al. 2002). We prefer the backflow/buoyancy model because, in our view, the

observed structures of X-shaped radio galaxies are the natural consequences of strong backflows in an asymmetric medium, and there is no indication that the lobes of 3C 403 are highly overpressured.

We know that strong backflows exist in radio galaxies, and that there are many cases in which the morphology of the ambient medium in clusters, groups, and isolated elliptical galaxies is complex. The dynamics of the backflow of material from the jet head are determined by several factors, including the jet velocity, the density contrast between the jet and the ambient medium, and the temperature and density profiles of the medium into which the jet is propagating (Leahy & Williams 1984; Hardee et al. 1992). In particular, lighter jets (i.e., jets with a larger values of ρ_{ISM}/ρ_{jet}) have more powerful backflows than heavier jets. Backflow velocities ranging from several thousand km s^{-1} to $0.1c$ have been estimated for a sample of double-lobed 3CRR radio galaxies (Alexander & Leahy 1987). Thus, backflow velocities can be orders of magnitude higher than the advance speed of the jet head. Once the backflow material reaches a strong pressure gradient, it will rapidly decelerate and bend (depending on the details of the gradient), and subsequently it will be driven primarily by buoyancy forces (i.e., subsonically). The density and pressure morphologies of the hot gas in clusters, groups, and elliptical galaxies are complex. If *Chandra* observations of clusters of galaxies are any guide, there are no such things as spherically symmetric gas halos sitting idly in their gravitating dark matter potentials (M. Markevitch 2004, private communication). In our view, there is no compelling reason to invoke more complex phenomena, such as merging supermassive black holes, to explain X-shaped radio galaxies.

The arguments against the hydrodynamic models are based primarily on three considerations: the radio morphology of these objects, evidence for recent mergers, and radio spectral differences of the wings and lobes. None of these are strong arguments in our view, and we suggest that it is quite plausible (and even natural) for backflow/buoyancy to create the structures that are observed. The most important of the three are those based on the radio morphology. In some sources, the wings (in projection) are longer than the lobes (as is the case in 3C 403, Dennett-Thorpe et al. 2002), and in others the alignment of the wings and lobes relative to the nucleus is sometimes offset (e.g., NGC 326, Gopal-Krishna et al. 2003). Qualitative arguments are often made that the observed morphologies are unlikely to be generally formed by hydrodynamic flows. The implicit assumption in these arguments is that the gas atmosphere that the jet is propagating into is roughly spherically symmetric. The observed radio structures will depend critically on the distribution of the gas into which the jet is propagating. Similarly, the general paradigm suggests that the lobes of FR II galaxies are advancing supersonically into the ambient medium, and it has been argued that it is not plausible that the wings and lobes are approximately the same length if the

lobes are evolving supersonically and the wings buoyantly (Leahy & Parma 1992). This claim is true *if* the lobes are advancing supersonically into the ambient medium, but there is no direct evidence to support this claim. In all cases in which the internal and external pressures of FR II lobes have been measured to date, the lobes appear to be close to pressure equilibrium with their surroundings, as we observe in 3C 403 (Hardcastle et al. 2002; Belsole et al. 2004; Croston et al. 2004), implying relatively slow expansion. The complex radio morphology of 3C 403 is clearly different from the canonical lobe/hot spot morphology of classic FR II radio galaxies, such as Cyg A, and its radio luminosity lies on the FR I/FR II dividing line. Both of these suggest that 3C 403 is among the least powerful sources in this class. The inner radio lobes of M87, a radio galaxy on the FR I/FR II luminosity boundary, have detached from the shock propagating through the ICM of the Virgo cluster and are therefore evolving buoyantly and subsonically (Forman et al. 2005).

In addition, some have argued that there is evidence for recent mergers in the host galaxies of some of these sources. This is certainly not a general conclusion, as 3C 403, one of the best-studied X-shaped radio galaxies, resides in a relatively poor environment and shows little evidence for a recent (within the last $\sim 10^8$ yr) merger. *HST* observations of the host galaxy of 3C 403 indicate the presence of weak dust lanes, suggestive of a much older merger, certainly older than the age of the radio source, estimated to be ~ 16 Myr based on radio spectral analysis (Dennett-Thorpe et al. 2002). Finally, multispectral radio observations of several winged sources (e.g., NGC 326 [Ekers et al. 1978] and B2 0828+32 [Klein et al. 1995]) suggest that the plasma in the wings is considerably older than that in the lobes. Variations in radio spectral index across the wings and lobes would be a natural result if the jet axis were slowly precessing. However, this observational result is also consistent with the hydrodynamic backflow models, in our view, for two reasons. First, the plasma in the wings is naturally older than that in the lobes, since it traveled back from the jet head to its present location in the wings. Second, the evolutionary history of the material in the wings is clearly different from that of the material currently in the lobes in the backflow model. The spectral differences could well be telling us something about the hydrodynamics and the nature of shock acceleration of the backflow and be unrelated to radiative energy loss of the most energetic particles. It is impossible to draw definitive conclusions from spectral differences between the wings and lobes.

The quality of our data presented in this paper is not sufficient for us to put strong constraints on the dynamics of the lobes/wings interaction with the ISM and make a definitive, general statement regarding the nature of X-shaped radio galaxies. We have detected nonaxisymmetric structures in the central region of the host galaxy. This result is consistent with the various hydrodynamic scenarios that have been invoked to explain this phenomenon. Deeper observations of this object and others with *Chandra* and/or *XMM-Newton* are required to better understand the interaction between the gaseous corona and the radio lobes in order to resolve this issue.

6. CONCLUSIONS

The primary results of this work include the following:

1. We have detected X-ray emission from the hot ISM, the active nucleus, several radio knots, and diffuse emission from the lobes and wings of the nearby X-shaped radio galaxy 3C 403.

2. Within ~ 5 kpc of the nucleus, the morphology of the hot gas is highly ($\epsilon \sim 0.57$) elliptic. This is consistent with the hypothesis that the X-shaped radio morphology is the result of the propagation of jets in nonaxisymmetric atmospheres. The distribution of the stars in the central 5 kpc is considerably less elliptical ($\epsilon \sim 0.2$). Our data are not of sufficient quality for us to make a good measurement of the density/pressure profile of the hot gas on larger scales, but within the uncertainties, the lobes and wings are in approximate pressure equilibrium with the hot corona.

3. We have detected X-ray and optical emission from radio knots and hot spots. Based on their radio/optical/X-ray spectra, we attribute the emission in all cases to synchrotron emission, not IC scattering from the CMB. All lines of evidence suggest that the jet and radio lobes lie at a large angle to the line of sight, so the effects of relativistic beaming are negligible. This is one of the best examples to date of synchrotron X-ray emission from the compact radio features of a narrow-line FR II radio galaxy.

4. The X-ray spectrum of the nucleus is well modeled by two power laws plus a broad, fluorescent Fe line from cold material. The first power law is heavily absorbed and is buried deeply in the torus. The second power law is less heavily absorbed, and we attribute this to X-ray emission from an unresolved jet. The ratio of X-ray–to–radio flux is consistent with that measured for the nuclei of other radio galaxies.

5. Diffuse X-ray emission is detected from the lobes and wings. This emission can generally be explained as IC scattering from the CMB if we assume moderate departure from equipartition.

REFERENCES

Alexander, P., & Leahy, J. P. 1987, MNRAS, 225, 1
Barthel, P. D. 1989, ApJ, 336, 606
Belsole, E., Worrall, D. M., Hardcastle, M. J., Birkinshaw, M., & Lawrence, C. R. 2004, MNRAS, 352, 924
Black, A. R. S., Baum, S. A., Leahy, J. P., Perley, R. A., Riley, J. M., & Scheuer, P. A. G. 1992, MNRAS, 256, 186
Brunetti, G., Bondi, M., Comastri, A., & Setti, G. 2002, A&A, 381, 795
Brunetti, G., Setti, G., & Comastri, A. 1997, A&A, 325, 898
Canizares, C. R., Fabbiano, G., & Trinchieri, G. 1987, ApJ, 312, 503
Canosa, C. M., Worrall, D. M., Hardcastle, M. J., & Birkinshaw, M. 1999, MNRAS, 310, 30
Capetti, A., Zamfir, S., Bodo, G., Zanni, C., & Massaglia, S. 2002, A&A, 394, 39
Carilli, C. L., Perley, R. A., & Harris, D. E. 1994, MNRAS, 270, 173
Comastri, A., Brunetti, G., Dallacasa, D., Bondi, M., Pedani, M., & Setti, G. 2003, MNRAS, 340, L52
Croston, J. H., Birkinshaw, M., Hardcastle, M. J., & Worrall, D. M. 2004, MNRAS, 353, 879
Davis, J. 2001, ApJ, 562, 575
Dennett-Thorpe, J., Scheuer, P. A. G., Laing, R. A., Bridle, A. H., Pooley, G. G., & Reich, W. 2002, MNRAS, 330, 609
Ekers, R. D., Fanti, R., Lari, C., & Parma, P. 1978, Nature, 276, 588
Evans, D. A., Kraft, R. P., Worrall, D. M., Hardcastle, M. J., Jones, C., Forman, W. R., & Murray, S. S. 2004, ApJ, 612, 786
Forman, W. R., et al. 2005, ApJ, in press
Gopal-Krishna, Biermann, P. L., & Wiita, P. J. 2003, ApJ, 594, L103
Govoni, F., Falomo, R., Fasano, G., & Scarpa, R. 2000, A&A, 353, 507
Hardcastle, M. J., Alexander, P., Pooley, G. G., & Riley, J. M. 1998a, MNRAS, 296, 445
———. 1999, MNRAS, 304, 135
Hardcastle, M. J., Birkinshaw, M., & Worrall, D. M. 1998b, MNRAS, 294, 615

Hardcastle, M. J., Birkinshaw, M., & Worrall, D. M. 2001, MNRAS, 326, 1499
Hardcastle, M. J., Harris, D. E., Worrall, D. M., & Birkinshaw, M. 2004, ApJ, 612, 729
Hardcastle, M. J., Worrall, D. M., Birkinshaw, M., Laing, R. A., & Bridle, A. H. 2002, MNRAS, 334, 182
Hardcastle, M. J., Worrall, D. M., Kraft, R. P., Forman, W. R., Jones, C., & Murray, S. S. 2003, ApJ, 593, 169
Hardee, P. E., White, R. E., Norman, M. L., Cooper, M. A., & Clarke, D. A. 1992, ApJ, 387, 460
Harris, D. E., et al. 1998, ApJ, 499, L149
———. 2000, ApJ, 530, L81
Heavens, A. F., & Meisenheimer, K. 1987, MNRAS, 225, 335
Heinz, S., Reynolds, C. S., & Begelman, M. C. 1998, ApJ, 501, 126
Isobe, N., Tashiro, M., Makishima, K., Iyomoto, N., Suzuki, M., Murakami, M. M., Mori, M., & Abe, K. 2002, ApJ, 580, L111
Klein, U., Mack, K.-H., Gregorini, L., & Parma, P. 1995, A&A, 303, 427
Kraft, R. P., Forman, W. R., Jones, C., Murray, S. S., Hardcastle, M. J., & Worrall, D. M. 2002, ApJ, 569, 54
Kraft, R. P., Vázquez, S., Forman, W. R., Jones, C., Murray, S. S., Hardcastle, M. J., Worrall, D. M., & Churazov, E. C. 2003, ApJ, 592, 129
Laing, R. A., Riley, J. M., & Longair, M. S. 1983, MNRAS, 204, 151
Leahy, D. A., & Creighton, J. 1993, MNRAS, 263, 314
Leahy, J. P., Black, A. R. S., Dennett-Thorpe, J., Hardcastle, M. J., Komissarov, S., Perley, R. A., Riley, J. M., & Scheuer, P. A. G. 1997, MNRAS, 291, 20

Leahy, J. P., & Parma, P. 1992, in Proc. 7th IAP Meeting, Extragalactic Radio Sources: From Beams to Jets, ed. J. Roland, H. Sol, & G. Pelletier (Cambridge, Cambridge Univ. Press), 307
Leahy, J. P., & Williams, A. G. 1984, MNRAS, 210, 929
Marshall, H. L., Miller, B. P., Davis, D. S., Perlman, E. S., Wise, M., Canizares, C. R., & Harris, D. E. 2002, ApJ, 564, 683
Martel, A., et al. 1999, ApJS, 122, 81
Merritt, D., & Ekers, R. D. 2002, Science, 297, 1310
Miyazaki, S., et al. 1996, PASJ, 48, 801
O'Sullivan, E., Forbes, D. A., & Ponman, T. J. 2001, MNRAS, 328, 461
Sambruna, R. M., Urry, C. M., Tavecchio, F., Maraschi, L., Scarpa, R., Chartas, G., & Muxlow, T. 2001, ApJ, 549, L161
Schlegel, D. J., Finkbeiner, D. P., & Davis, M. 1998, ApJ, 500, 525
Tadhunter, C. N., Morganti, R., di Serego-Alighieri, S., Fosbury, R. A. E., & Danziger, I. J. 1993, MNRAS, 263, 999
Tadhunter, C. N., Morganti, R., Robinson, A., Dickson, R., Villar-Martin, M., & Fosbury, R. A. E. 1998, MNRAS, 298, 1035
Tavecchio, F., Maraschi, L., Sambruna, R. M., & Urry, C. M. 2000, ApJ, 544, L23
Turner, T. J., George, I. M., Nandra, K., & Mushotzky, R. F. 1997, ApJ, 488, 164
Wilson, A. S., Young, A. J., & Shopbell, P. L. 2001, ApJ, 547, 740
Worrall, D. M., Birkinshaw, M., & Cameron, R. A. 1995, ApJ, 449, 93
Worrall, D. M., Birkinshaw, M., & Hardcastle, M. J. 2001, MNRAS, 326, L7